# Estimates of Air–Sea Feedbacks on Sea Surface Temperature Anomalies in the Southern Ocean

Ute Hausmann

*Department of Earth, Atmospheric and Planetary Sciences, Massachusetts Institute of Technology, Cambridge, Massachusetts*

Arnaud Czaja

*Department of Physics, Imperial College London, London, United Kingdom*

John Marshall

*Department of Earth, Atmospheric and Planetary Sciences, Massachusetts Institute of Technology, Cambridge, Massachusetts*

## ABSTRACT

Sea surface temperature (SST) air–sea feedback strengths and associated decay time scales in the Southern Ocean (SO) are estimated from observations and reanalysis datasets of SST, air–sea heat fluxes, and ocean mixed layer depths. The spatial, seasonal, and scale dependence of the air–sea heat flux feedbacks is mapped in circumpolar bands and implications for SST persistence times are explored. It is found that the damping effect of turbulent heat fluxes dominates over that due to radiative heat fluxes. The turbulent heat flux feedback acts to damp SSTs in all bands and spatial scales and in all seasons, at rates varying between 5 and $25 \, \mathrm{W \, m^{-2} \, K^{-1}}$, while the radiative heat flux feedback has a more uniform spatial distribution with a magnitude rarely exceeding $5 \, \mathrm{W \, m^{-2} \, K^{-1}}$. In particular, the implied net air–sea feedback (turbulent + radiative) on SST south of the polar front, and in the region of seasonal sea ice, is as weak as $5$–$10 \, \mathrm{W \, m^{-2} \, K^{-1}}$ in the summertime on large spatial scales. Air–sea interaction alone thus allows SST signals induced around Antarctica in the summertime to persist for several seasons. The damping effect of mixed layer entrainment on SST anomalies averages to approximately $20 \, \mathrm{W \, m^{-2} \, K^{-1}}$ across the ACC bands in the summer-to-winter entraining season and thereby reduces summertime SST persistence to less than half of that predicted by air–sea interaction alone (i.e., 3–6 months).

## 1. Introduction

It has long been known that midlatitude SST anomalies tend to be damped by air–sea interaction at a rate of, typically, $\alpha \approx 20 \, \mathrm{W \, m^{-2} \, K^{-1}}$ (Frankignoul 1985; Frankignoul et al. 1998). Thus, if an SST anomaly extends over a mixed layer depth, say $h = 50 \, \mathrm{m}$, it will decay on a time scale of $\tau = \rho_0 c_p h / \alpha \approx 4$ months, where $\rho_0$ is the density of seawater and $c_p$ is its specific heat. The air–sea heat flux feedback $\alpha$ is an important parameter. For example, it represents the thermal surface boundary condition for ocean-only model integrations. The latter routinely employ a constant $\alpha$. However, as shown from observations by Frankignoul et al. (1998), Frankignoul and Kestenare (2002, hereinafter FK02) and Park et al. (2005), $\alpha$ is not constant, but instead varies in space and time as well as with spatial scale. Midlatitude air–sea feedbacks are observed to feature a systematic seasonal dependence, being typically larger in fall and winter. Moreover they exhibit considerable spatial structure, increasing toward the western margins of ocean basins, where large air–sea contrasts are maintained by the continuous supply of (cold and dry) continental air. In the tropics feedbacks are observed to be weaker than in middle latitudes.

Air–sea feedbacks in closed basins and over (western) boundary current regimes are reasonably well documented in the Northern Hemisphere (NH), as well as in

*Corresponding author address*: Ute Hausmann, Department of Earth Atmospheric and Planetary Sciences, Massachusetts Institute of Technology, Green Bldg., 77 Massachusetts Ave., Cambridge, MA 02139.
E-mail: uhaus@mit.edu

the low latitudes of the Southern Hemisphere (SH). In the Southern Ocean (SO), however, feedback strengths are not yet constrained from observations. The SO with its Antarctic Circumpolar Current (ACC) plays a critical role in the climate system. In this large expanse of open ocean, spanning from the subtropical basins all the way to the region of seasonal sea ice around Antarctica and featuring the special geometry of a circumpolar channel, air–sea feedbacks may differ from those operating in midlatitude basins. Moreover, in addition to weather systems, SO SST variability is largely driven by the southern annular mode (SAM), the primary mode of atmospheric variability in the middle-to-high-latitude Southern Hemisphere (SH). The SAM induces SST anomalies on larger-than-synoptic spatial scales, typically characterized by a few poles along the circumpolar channel (e.g., Verdy et al. 2006; Ciasto and Thompson 2008). Given the possible link between observed trends in the SAM and anthropogenic perturbations of climate, by greenhouse gases and stratospheric ozone (e.g., Thompson et al. 2011), the fate of these large-scale SAM-induced SST anomalies is of particular interest, as it determines their potential influence on recent observed SH climate trends. Indeed, coupled modeling studies examining the response of SO SST and Antarctic sea ice to SAM, and relatedly, ozone hole forcing, show large discrepancies and identify their modeled air–sea SST feedbacks as one of the primary sources of uncertainty in the models' SST responses (Ferreira et al. 2015). This urgently calls for observation-based estimates of air–sea feedbacks in the SO.

As discussed by Bretherton (1982), Frankignoul (1985), Rahmstorf and Willebrand (1995), Bladé (1997), and Ferreira et al. (2001), among others, air–sea damping of SST anomalies is expected to depend on their spatial scale. If the lateral scale of SST anomalies is sufficiently large, the temperature of the marine atmospheric boundary layer has time to adjust to their presence, minimizing the air–sea temperature difference and thus reducing the magnitude of the negative feedback. For example, FK02 show a weakening of $\alpha$ in the NH basins, by typically 5–10 W m$^{-2}$ K$^{-1}$, moving from synoptic to basin scales. They establish that even on basin scales the feedback is provided by the response of turbulent fluxes to SST, which exceeds the radiative response by an order of magnitude. The strongest adjustment and thus weakest damping is expected for basin-wide SST anomalies. The implications of this for the fate of SST anomalies that span the entire circumpolar extent of the ACC remain to be assessed.

In this paper, we propose to exploit the most recent available observational datasets and atmospheric reanalysis products of SO air–sea interactions and mixed layer depths, to diagnose air–sea feedback strengths and

associated SST damping time scales in the SO as a function of spatial scale. We present estimates of $\alpha$ and $\tau$ across the SO, explore their spatial patterns and seasonal variability, and discuss the implications for SST persistence times as a function of season and scale, and thus our understanding of SH climate variability. A particular focus will thereby be placed on the damping time scales of large-scale SST anomalies generated around Antarctica in the summer season, during which large recent-decade upward trends in SH westerlies, and thus in surface Ekman advection perturbing SST, have been linked to stratospheric ozone perturbations (e.g., Thompson et al. 2011).

The paper is set out as follows. Section 2 introduces datasets and methods. Thereafter section 3 presents our new estimate of the air–sea feedback in the SO. Its seasonality and the associated air–sea damping time scales are discussed in section 4, and in section 5 we analyze the dependence of SO air–sea feedbacks and damping time scales on spatial scale. A discussion of the implications of these results for SH SST variability and its physical mechanisms is provided in section 6. Conclusions are presented in section 7.

## 2. Data and methods

The feedback between anomalies in air–sea heat fluxes ($Q$, positive upward) and SST ($T$) is given by

$$\alpha \equiv \left.\frac{\partial \langle Q' \rangle}{\partial T'}\right|_{\overline{T}}. \tag{1}$$

Here primes indicate departures from the seasonal background state (denoted by overbars) and $\langle Q' \rangle$ denotes the systematic heat flux response to a given perturbation in SST that is to be isolated (e.g., by composite averaging over a large range of different atmospheric conditions) from other sources of variability in $Q'$ such as the (essentially random) atmospheric synoptic variability. Positive values of $\alpha$, representing anomalous heat loss (gain) over warm (cold) SST anomalies, thus correspond to a negative heat flux–SST feedback, which damps the SST anomaly at its origin.

Over the SO, air–sea heat fluxes remain poorly observed resulting in a large spread between available estimates (e.g., Bourassa et al. 2013). Given the need for observational constraints on SO air–sea damping rates outlined in section 1, here we attempt to provide observational estimates for $\alpha$ in the SO by comparing two of the available datasets of monthly turbulent (latent + sensible) and radiative (net longwave + net shortwave) air–sea heat fluxes $Q$. The first is the ECMWF interim reanalysis (ERA-Interim, hereinafter ERA-I; Dee et al. 2011), which we analyze in its 0.75° grid version during

the 34-yr period September 1979–August 2013. The second is OAFlux, which estimates turbulent fluxes (on a 1° grid) by applying COARE, version 3.0, bulk formulas to daily objectively analyzed air–sea state variables and merges available satellite data with three atmospheric reanalyses (Yu et al. 2008; http://oaflux.whoi.edu). We restrict the analysis of OAFlux to post-January 1985 thereafter satellite SSTs are assimilated, resulting in 29 years (1985–2013) of turbulent fluxes and 25 years (1985–2009) of radiative fluxes, the latter obtained from the International Satellite Cloud Climatology Project (ISCCP) and provided alongside OAFlux. In the analysis, we use SST from the respective dataset for consistency and obtain primes as departure from the monthly climatology as estimated for each dataset's available record. Whereas OAFlux is provided for the ice-free ocean only, the partitioning of reanalysis surface heat fluxes into air–sea and air–ice fluxes is not straightforward in regions of sea ice. We thus experimented with several methods to prevent contamination of $Q$, the air–sea heat fluxes whose feedbacks on SST are to be estimated, by air–ice fluxes. Here we choose to mask $Q$ within the reanalysis's climatological sea ice edge, defined in the following using a 15% threshold on the sea ice concentration $c$. Additionally a more stringent $c > 0\%$ masking criterion for $Q$ is used at times to evaluate any possible effects of residual contamination. Note that ocean–sea ice heat fluxes are anticipated to provide a negative feedback on any wintertime SST anomalies in the region of seasonal sea ice, operating in addition to the negative air–sea (i.e., ocean–atmosphere) heat flux SST feedback, which we estimate here. We do not attempt to quantify this ocean–ice heat flux feedback on SST in this study. The northern limit of the analysis domain is chosen to be 30°S.

Air–sea heat fluxes play a key role in the generation of SST anomalies, especially on the spatial scale of atmospheric synoptic disturbances. Estimating (1) then relies on separating the feedback from these forcing contributions to $Q'$. As pioneered by Frankignoul et al. (1998), this can be achieved by analyzing the lagged covariance between time series of $T'$ and $Q'$, where $Q'$ lags $T'$ by more than the atmospheric persistence time (see further discussion in appendix B). Here we follow this method, as refined by FK02 and applied to reanalyses and observations by FK02 and Park et al. (2005). Accordingly we estimate (1) as

$$\alpha = \frac{1}{n} \sum_{i=1}^{n} \frac{\overline{T'(t)Q'(t+i\delta t)}}{\overline{T'(t)T'(t+i\delta t)}}, \tag{2}$$

that is, as the $T'$–$Q'$ covariance at positive lags ($Q'$ lags), weighted by the decay of $T'$ itself and averaged over lags

from 1 to $n\delta t$ (here $\delta t$ is 1 month). The time averaging in (2), denoted by overbars, thereby enables us to identify the systematic heat flux response to a given perturbation in SST, as denoted by $\langle \ \rangle$ in (1).

In section 3, we estimate (2) from year-round time series (i.e., using all 12 months of the year). In this case, following FK02, $n$ is set to 3 or, if smaller, to the maximum lag for which the $T'$ autocorrelation is larger than zero at a confidence level of 95% (if the latter criterion is not met for $i = 1$, $\alpha$ is not estimated at that location). Section 4 also uses (2) to estimate feedbacks seasonally. In this case, $n$ is set to 1 and only certain months of the year are included in time $t$ in (2). For example, $\alpha$ in December–February (DJF), which we denote $\alpha$DJF, is obtained taking $t$ only in November–February (NDJF), that is from NDJF $T'$ and lag $i = 1$ [i.e., December–March (DJFM)] $Q'$ time series. (Note that throughout this paper uppercase letter combinations, such as DJF, refer to the first letters of the months of the year included in the seasonal feedback estimates.)

The estimate (2) for the air–sea feedback is rooted in the theoretical framework of stochastic climate models (e.g., Frankignoul and Hasselmann 1977), and its efficacy depends on atmospheric persistence times being small (less than one month, i.e., $1\delta t$). If $Q'$ is a primary forcing agent of $T'$, any lower-frequency contributions to $Q'$, other than that induced by its response to $T'$, will bias estimates based on (2) toward a positive feedback (cf. FK02). To minimize this effect, prior to evaluating (2), we remove from the anomaly time series, first, linear seasonal trends over the analysis time span (estimated separately for each month of the year) and, second, a linear seasonal ENSO signal (as in FK02, and defining ENSO as the Niño-3.4 index obtained from each dataset's detrended $T'$). As further discussed in appendix A, the covariance function of the resulting $T'$ and $Q'$ time series based on ERA-I and OAFlux data indeed changes sign between negative and positive lags across a wide range of spatial scales throughout the SO, showing that a clear feedback signal can be isolated by the application of (2). Error in the estimate of $\alpha$ stems from both the error on $T'$ and $Q'$ data, which is poorly known [while the OAFlux report (Yu et al. 2008) estimates a mean error on the long-time annual-mean turbulent $Q'$ varying from approximately 5 to $15\,W\,m^{-2}\,K^{-1}$ on moving equatorward across the SO, a comparison to in situ measurements of $Q'$ in the SO is lacking and the error on the time variability of $Q'$ remains uncertain], as well as from the error due to the uncertainty in the estimate (2) from short time series. The latter is quantified in appendix B and is found to be typically 50% of the estimated feedback strength.
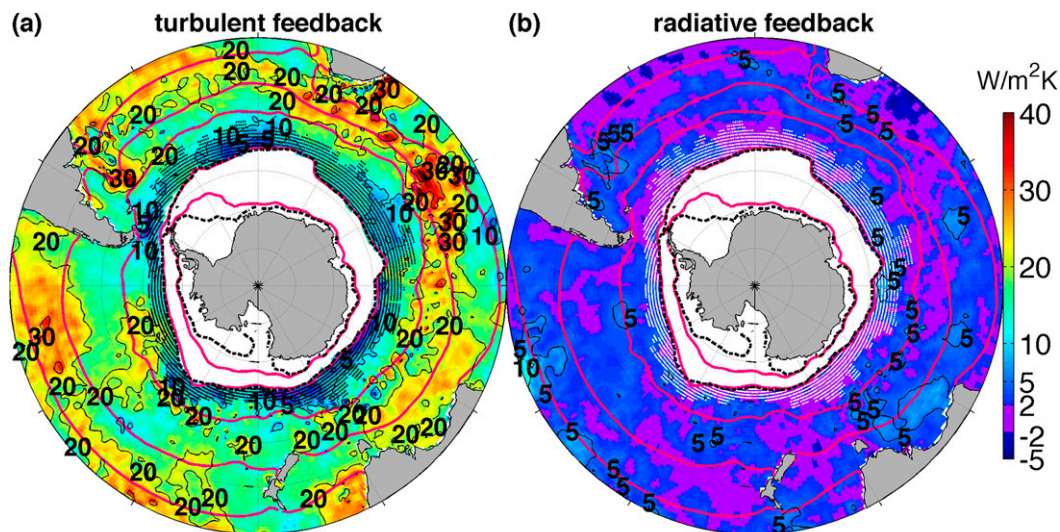
FIG. 1. SO (a) turbulent and (b) radiative feedback strength $\alpha$ (W m$^{-2}$ K$^{-1}$) estimated from ERA-I data using (2). Bright red contours show, starting at the pole, the February 0°C, October −1°, 5.5°, 11°, and 16.5°C climatological SST isotherms. Dashed black contours show, also starting at the pole, the 15% isolines of the February and October climatological sea ice concentration $c$. Stippling (black or white, for better visibility) indicates regions, in which the estimate of $\alpha$ would be unavailable if only based on $Q$ with $c > 0\%$ (rather than $c > 15\%$ as colored).

To relate the estimated feedback to SSTA damping rates (sections 4 and 5), we use a large-scale (0.5°) monthly climatology of the mixed layer depth $\bar{h}$. It is derived by Schmidtko et al. (2013) by applying a density-based mixed layer depth identification algorithm (as developed by Holte and Talley 2009) to individual, highly resolved hydrographic profiles, collected by Argo floats and ships pre-2011. A subsequent refined objective mapping procedure is designed to yield a climatology representative of the large-scale 2007–11 state. (We use version 2.2 of the optimal interpolation mixed layer ocean climatology provided at www.pmel.noaa.gov/mimoc/.) Note that overall conclusions are not sensitive to the choice of this climatology, and qualitatively similar results are obtained when using more traditional temperature or density threshold–based mixed layer climatologies (as provided e.g., by de Boyer Montégut et al. 2004; de Boyer Montégut 2008; Dong et al. 2008).

## 3. SO air–sea feedback strength

Figure 1a displays the SO feedback of turbulent (latent + sensible) air–sea heat fluxes on SST anomalies $\alpha_{turb}$ estimated from ERA-I data following (2). We see that the turbulent air–sea feedback $\alpha_{turb}$ has a typical magnitude of approximately 15 W m$^{-2}$ K$^{-1}$ in the SO. It features a broad latitudinal dependence decaying from larger values in the SH midlatitudes ($\sim$20–30 W m$^{-2}$ K$^{-1}$) toward smaller values around the

ACC. Note the circumpolar band sandwiched between the October-time 5.5°C surface isotherm and the wintertime sea ice edge at −1°C (both shown in red contours). Here $\alpha \approx 10$ W m$^{-2}$ K$^{-1}$ and less. In contrast the net radiative air–sea feedback $\alpha_{rad}$, displayed in Fig. 1b, shows uniformly low values (of typically $\sim$0–5 W m$^{-2}$ K$^{-1}$) across the entire SO. Figure 1 thus indicates that in the SO, just as in the NH midlatitude basin interiors (FK02; Park et al. 2005), the net air–sea feedback is negative (positive values of $\alpha$), and dominated by turbulent air–sea heat exchanges. As Antarctica is approached $\alpha$ falls from typical midlatitude values of 20–30 W m$^{-2}$ K$^{-1}$ to approximately 10 W m$^{-2}$ K$^{-1}$.

In the SH midlatitudes (equatorward of 40°S), the high values of the net air–sea feedback, as well as the near-zero radiative contribution to them, agree with the estimate provided previously for this region from NCEP reanalysis data by Frankignoul et al. (2004). Around Antarctica, to minimize the contribution of air–ice fluxes to $Q$ and to the estimate of the air–sea heat flux feedback $\alpha$, the latter (colored in Fig. 1) is only based on data points of $Q$, for which the sea ice concentration $c \leq$ 15%. The stippling in Fig. 1 moreover indicates where an estimate of $\alpha$ based on an even more stringent criterion, including $Q$ only for $c = 0\%$, would be unavailable. In these stippled regions, characterized by occasional low area-concentration sea ice cover, a residual contamination of the estimate of $\alpha$ by air–ice heat flux contributions to reanalysis surface heat fluxes thus cannot be excluded. More discussion of the sensitivity of
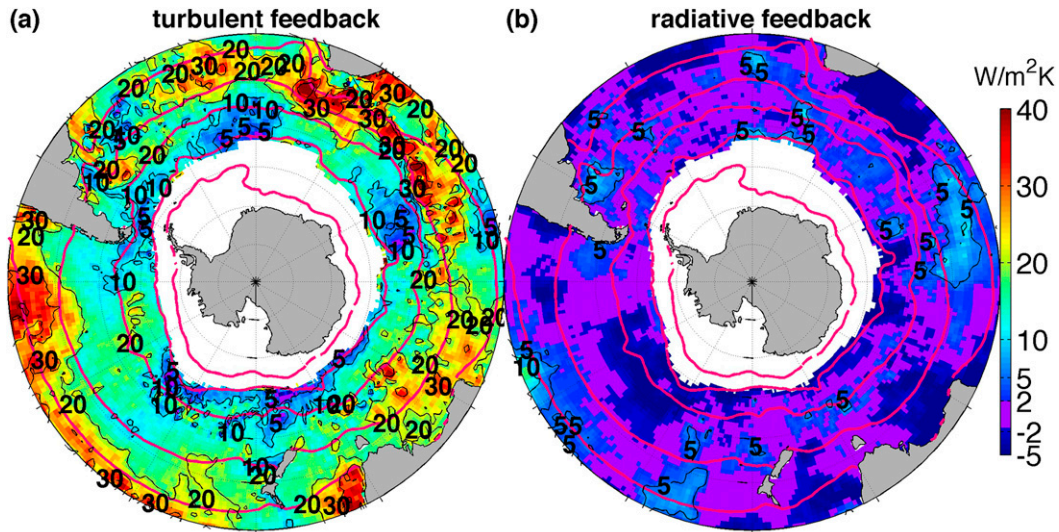
FIG. 2. As in Fig. 1, but estimated from OAFlux data. Here bright red contours show OAFlux-based climatological SST isotherms, namely, starting at the pole, the February 0.5°C and October 0°, 5.5°, 11°, and 16.5°C.

our results to the choice of concentration threshold is provided below (together with the discussion of Fig. 5).

To provide further confidence in the estimate poleward of 40°S, the analysis has been repeated with OAFlux data, as described in section 2. The estimate based on OAFlux is displayed in Fig. 2, and agrees well with that based on ERA-I (Fig. 1), in overall magnitude, spatial distribution, and its partition between turbulent and radiative fluxes. Differences include larger high and low extremes in OAFlux's turbulent feedback (Fig. 2a) and a more patchy map of OAFlux's $\alpha_{rad}$ with extensive regions of a weakly positive radiative feedback (Fig. 2b). Importantly, the low net air–sea feedback found along the path of the ACC in Figs. 1 and 2 (~10–15 W m$^{-2}$ K$^{-1}$) is robust across the two datasets, and contrasts with the higher net air–sea feedback (from 20 to ≥45 W m$^{-2}$ K$^{-1}$ locally) observed in the region of major current systems of the midlatitude ocean basins [as shown here and in the previous studies by FK02, Frankignoul et al. (2004), and Park et al. (2005)].

Figure 3 provides further analysis of the turbulent feedback in the SO, by separating out latent and sensible contributions. The sensible feedback is typically several times weaker and rarely exceeds 5 W m$^{-2}$ K$^{-1}$. Comparison with Fig. 1 reveals that latent air–sea heat fluxes indeed provide the bulk of the turbulent feedback and also set its poleward decrease. Sensible fluxes contribute to a peak in damping along the Agulhas Return Current and to a weaker maximum along the path of the ACC in the South Pacific. Figure 3c reveals a clear proportionality between latent and sensible feedback strengths. Their ratio

$r = \alpha_{sens}/\alpha_{lat}$ decreases systematically with background SST (indicated by the colors in Fig. 3c). Over the SH's warm midlatitude basin interiors and poleward western boundary currents (with winter temperatures in excess of 12°C), $r$ lies below ⅓ and can be as small as ¹⁄₁₀. In the cold ACC band (characterized by winter temperatures below 5.5°C), on the other hand, $r$ exceeds ½ and sensible fluxes contribute significantly (at least one-third) to the turbulent feedback. In regions of near-zero turbulent feedback encountered close to the sea ice edge, a clear proportionality between the two contributions is lost. The spatial variations of $r$ are robust across the two datasets we have examined (not shown).

## 4. SO air–sea damping time scales and seasonality

The seasonal variation of the turbulent air–sea feedback observed across the SO is displayed in Fig. 4a. Here each season's estimate for $\alpha_{turb}$ is obtained as described in section 2. Similar to previous observational results for the NH, SH midlatitudes feature a weaker turbulent feedback in spring and summer (SON and DJF) than in fall and winter (MAM and JJA), when winds are larger and $\alpha_{turb}$ often exceeds 30 W m$^{-2}$ K$^{-1}$. Over the higher-latitude SO, seasonality is not very pronounced. Nonetheless, pockets of elevated feedback (>25 W m$^{-2}$ K$^{-1}$) are observed particularly in winter (JJA), and a consistently weak feedback is encountered in summer (DJF). Especially in spring (SON), a peak in $\alpha_{turb}$ is discernible along the ACC path. Here, and in this season, SST variability is expected to contain a significant contribution
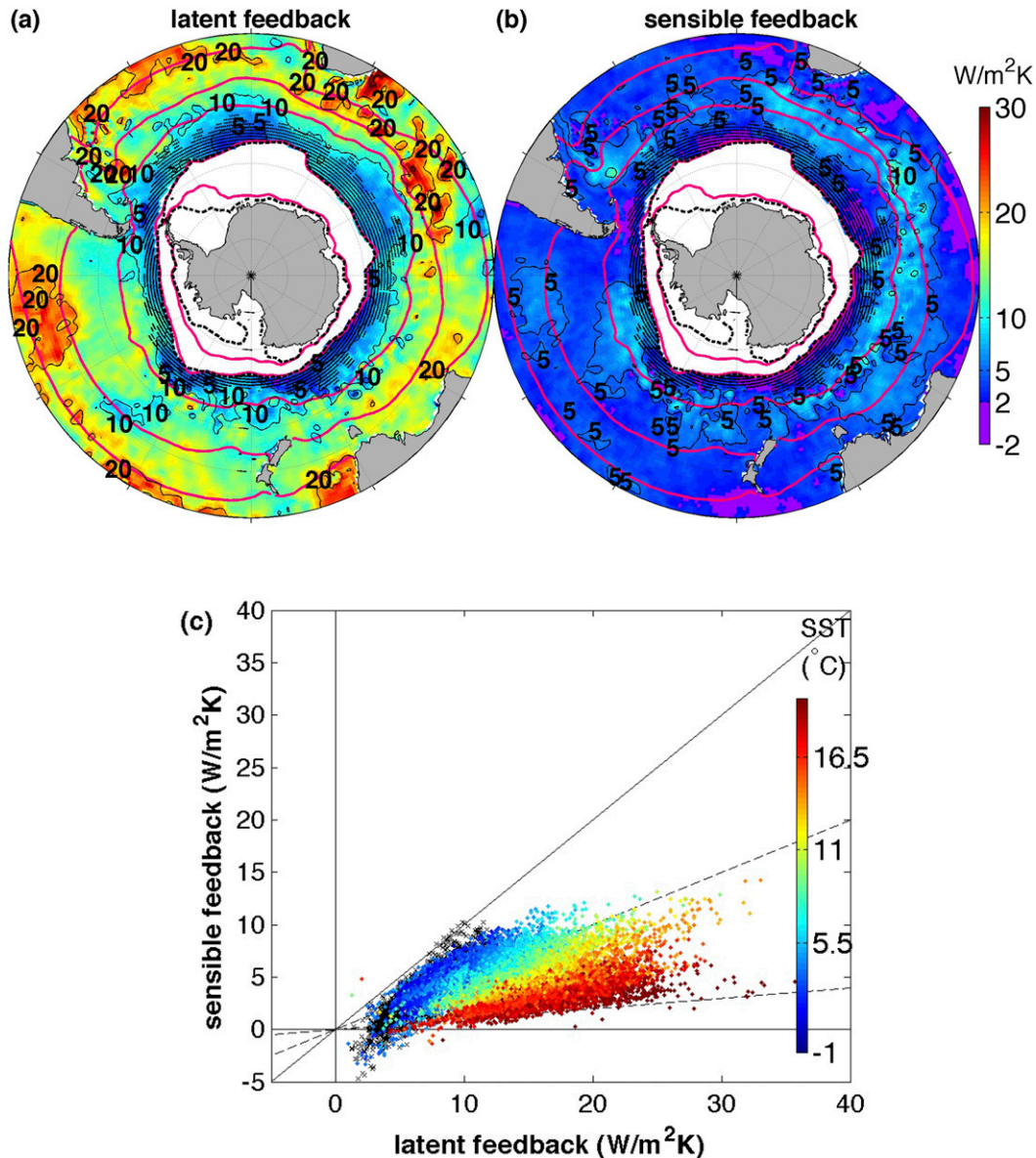
FIG. 3. SO (a) latent and (b) sensible contributions to the turbulent feedback (W m$^{-2}$ K$^{-1}$) estimated from ERA-I data. (c) Scatterplot of the data mapped in (b) against those in (a). The colors indicate October SST (°C). Starting from the top, lines display a ratio $\alpha_{\text{sens}}/\alpha_{\text{lat}}$ equal to 1, $^{1}/_{2}$, and $^{1}/_{10}$. Note that points stipled in (a),(b) are not colored, but indicated by black crosses in (c).

from the oceanic mesoscale (e.g., Hausmann and Czaja 2012). It is interesting to speculate that this peak may be a signature of the expected increase of $\alpha$ toward smaller spatial scales.

The radiative air–sea feedback $\alpha_{\text{rad}}$ for the four seasons is displayed in Fig. 4b. It is typically $\leq 5$ W m$^{-2}$ K$^{-1}$, with somewhat more expansive pockets of slightly larger values ($\sim 10$ W m$^{-2}$ K$^{-1}$) in spring and summer, but overall little seasonality. Radiative fluxes thus typically provide a negative feedback of much smaller magnitude than that provided by turbulent fluxes across the SO and throughout the year.

The general seasonal dependence of $\alpha_{\text{turb}}$ in the SO (Fig. 4a) is reproduced by the OAFlux estimate (not shown), which, similar to the year-round case (section 3), features larger (smaller) feedbacks where the feedback is large (small), by a few watts per meter squared per kelvin. The OAFlux/ISCCP-based estimate of seasonal radiative feedbacks (not shown) features more widespread positive feedbacks, of approximately $-5$ W m$^{-2}$ K$^{-1}$, across the
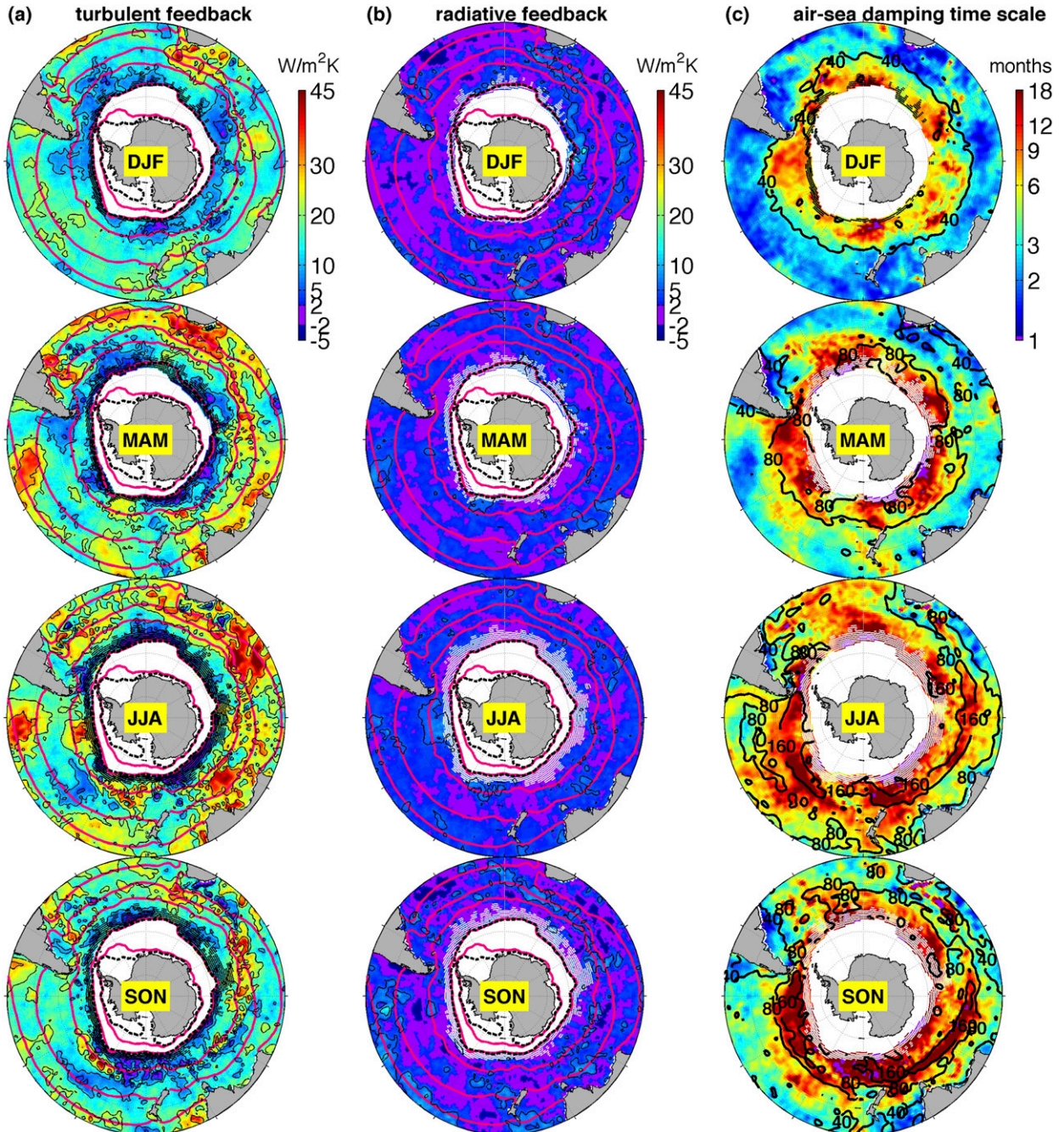
FIG. 4. (a),(b) As in Fig. 1, but for the four seasons (and with a modified color scale). (c) The associated air–sea damping time scale $\tau = \rho_o c_p \overline{h} / \alpha$ as indicated by the color scale (months), including both turbulent and radiative contributions to the feedback (i.e., using $\alpha = \alpha_{\text{turb}} + \alpha_{\text{rad}}$). The 40-, 80-, and 160-m isolines of each season's climatological mixed layer depth $\overline{h}$ are contoured. [The purple shading in (c) masks rare occurences of either $\tau < 1$ month or $\alpha < 2\,\text{W}\,\text{m}^{-2}\,\text{K}^{-1}$.]

SO in summer and spring. Besides being rather small it has little correlation with the ERA-I based estimate of Fig. 4b. This shows that our knowledge of SO radiative air–sea fluxes remains poor. Importantly for the purpose of this study, around the ACC and adjacent to the region of

seasonal sea ice, a weak net (turbulent + radiative) negative air–sea feedback of approximately 10–15 W m$^{-2}$ K$^{-1}$ is encountered year-round, and is provided mostly by turbulent fluxes, with little anticipated impact of the overall near-zero radiative air–sea feedback.

The associated air–sea damping time scale of SST anomalies $\tau = \rho_0 c_p \overline{h}/\alpha$, depends on $\rho_0 c_p \overline{h}$, the thermal inertia of the well-mixed surface layer that SST-induced air–sea heat fluxes act upon. A seasonal estimate for $\tau$, based on the $\overline{h}$ climatology introduced in section 2 and the seasonal turbulent + radiative feedbacks of Figs. 4a and 4b, is mapped in Fig. 4c. Observed SO $\tau$ range from 1 to >12 months and show a pronounced poleward and summer-to-wintertime increase.

The observed general increase in mixed layer depth from the subtropics toward the ACC region (from <40 to >160 m, as contoured) accentuates the effect of the observed poleward decrease of the air–sea feedback (Fig. 1a), leading to a pronounced increase of SST damping time scales from low latitudes (~1 month) to high latitudes (from 6 to >12 months, Fig. 4c). The seasonal cycle of mixed layer depth (characterized by deeper mixed layers in winter and spring), instead, works against and overrides the weaker seasonal cycle of the SO air–sea feedback. Thus, we observe shorter SST air–sea damping time scales over the shallower mixed layers despite the prevalence of the observed weak air–sea feedback during the summertime. Especially in winter and spring, damping time scales peak (>1 yr) together with mixed layer depths (>160 m) over the frontal regions of the ACC and its equatorward edge, leveling off at slightly reduced values (~9 months) farther poleward in the regions of less extreme winter mixing ($\overline{h} \geq 100$ m) yet low air–sea feedbacks approaching the sea ice edge. The key conclusion of Fig. 4c is that, in the (sea ice free) SO poleward of 50°S, air–sea interaction alone leads to damping time scales of SST anomalies longer than approximately 4–6 months everywhere and throughout the year.

## 5. SO air–sea feedback as a function of spatial scale

The above observational results apply to the air–sea feedback acting on spatial scales of SST variability as small as those resolved in the data, expected to lie somewhat above the grid scale. With a grid scale of 0.75°, the ERA-I data used here are likely to capture some remnants of ocean mesoscale variability (~100 km) and certainly adequately resolve the spatial scales of atmospheric synoptic disturbances (~1000 km). Given this information, what can we say about how strongly the overlying atmosphere damps dipolar, tripolar, or quadrupolar SST perturbations along the ACC, which are typically associated to SAM forcing (e.g., Verdy et al. 2006; Ciasto and Thompson 2008)? Previous studies reported a reduced damping on basin compared to synoptic scales in the NH (e.g., FK02), and we theoretically expect (Bretherton 1982;

Frankignoul 1985) such a weakening of the air–sea feedback as spatial scales expand. This might be expected to be particularly true in the SO, where zonal variations in air–sea properties are reduced due to the large downstream fetch of the ocean.

To estimate the air–sea feedback acting at spatial scales larger than a given threshold, the contribution of smaller scales needs to be eliminated from SST and heat flux variability. Here we carry out a simple spatial averaging of the data to coarser grids and then estimate $\alpha$ from these coarse-grained time series of $T'$ and $Q'$, in the same manner as described in section 2 for the grid scale. [Before applying (2), linear trends and ENSO-related low-frequency variability are removed from the coarse-grained time series.]

Figure 5a displays the result based on ERA-I data (two sets of filled markers, circles include $Q$ if the sea ice concentration $c \leq 15\%$, diamonds only if $c = 0\%$) averaged over three circumpolar streamline ranges, whose average latitude is indicated by the colors. Starting from the pole, these are defined as bounded by climatological October SST from $-1°$ to 5.5°C (spanning from the Antarctic wintertime sea ice edge to the northernmost surface isotherm passing through Drake Passage), 5.5°–11°C (equatorward branches of the ACC and mode-water regions), and 11°–16.5°C (SH subtropical interiors and Agulhas Return Current). These are the regions indicated by the bright red contours in, for example, Fig. 1.

For each band, the first point along the horizontal axis in Fig. 5 corresponds to $\alpha$ estimated from $T'$ and $Q'$ at the grid scale (as mapped in Fig. 1a) and then spatially averaged over all grid boxes lying within the respective isotherm band. Subsequent points correspond to $\alpha$ estimated from coarse-grained $T'$ and $Q'$, spatially averaged over all coarse grid boxes within a band. The meridional scale of the coarse boxes is thereby set by that of the band (~10° latitude), and the zonal scale is increased from 5° to 10°, 30°, 60°, 90°, 120°, 180°, and 360° longitude, at which point only one circumpolar box remains spanning each entire band. The horizontal axis of Fig. 5 indicates the resulting (band average) coarse-box area, in an area unit we refer to as SU, where 1 SU equals the area of a 10° latitude by 1° longitude box at 40°S. An area of 0.1 SU (1° latitude × 1° longitude) thus corresponds to roughly $100^2$ km$^2$, and areas of 10 and 100 SU (10° latitude × 10° and 100° longitude) correspond to $1000^2$ km$^2$ and 1000 km × 10 000 km.

Two realizations of the analysis are displayed at each scale, the second being obtained by shifting the center longitude of any given coarse box to the east by half its zonal extent (note that at grid and circumpolar scales only one realization is possible). Whereas at small scales the two realizations produce near-identical results, at
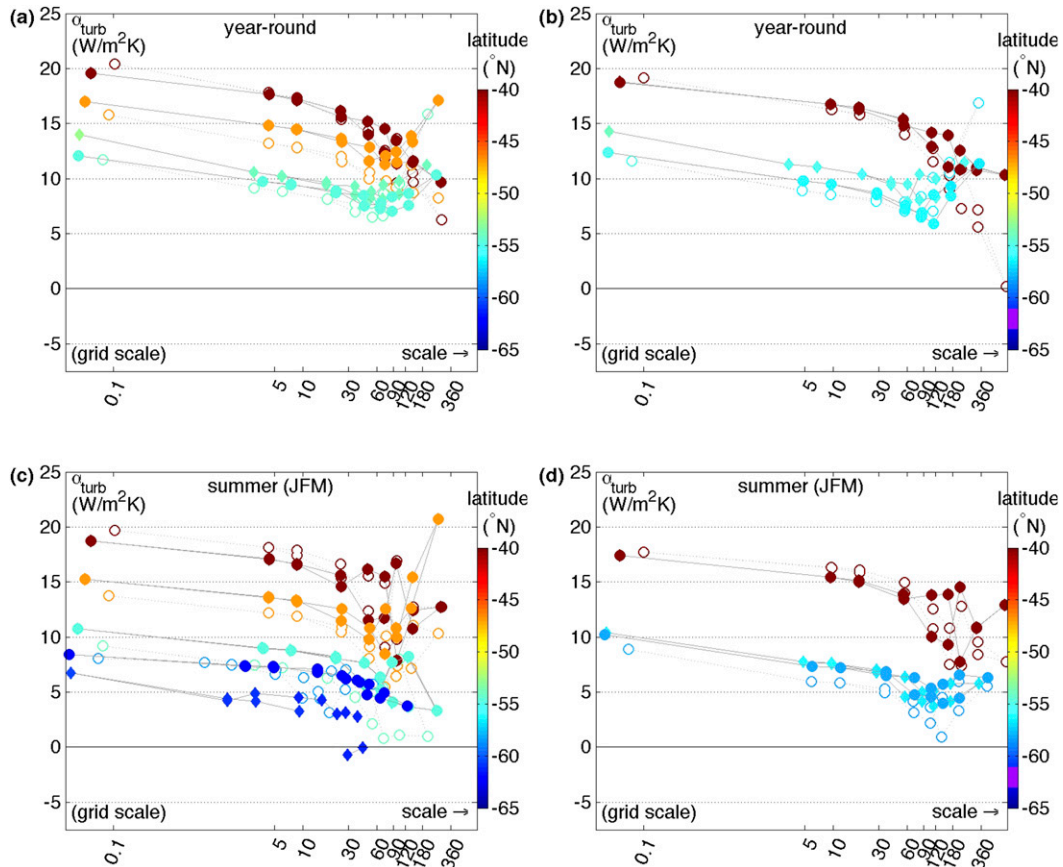
FIG. 5. SO turbulent air–sea feedback (vertical axes; $W\,m^{-2}\,K^{-1}$) as a function of spatial scale. Horizontal axes indicate area (SU), where 1 SU equals the area of a 1° longitude by 10° latitude strip at 40°S, with the grid scale, $\leq 1°$ × 1°, at $\leq 0.1$ SU. The estimate uses (2) applied to (a),(b) year-round and (c),(d) summertime $T'$ and $Q'$. ERA-I (filled markers) and OAFlux (open markers) data are used, each coarse grained to the respective scales within various circumpolar bands. The bands' average latitude is indicated by the warm to cold color scale on moving from low to high latitudes: (a),(c) the isotherm bands 16.5°–11°C, 11°–5.5°C, and from 5.5° to −1°C October SST; (b),(d) the latitude bands 30°–50°S and 50°–70°S. In (c), the −1°C October to 0°C February SST seasonal sea ice band (blue) is also shown (cf. bright red contours in Fig. 1). Note that for the OAFlux estimate the limits of the farthest poleward isotherm bands in (a) and (c) are the 0°C October and 0.5°C February OAFlux SST, corresponding most closely to the poleward edge of the year-round and summertime region of available OAFlux data (cf. bright red contours in Fig. 2). For ERA-I two sets of filled markers show the estimate obtained with $c > 15\%$ (circles) and $c > 0\%$ (diamonds) sea ice masking of $Q$.

scales larger than about 60°–90° longitude the estimates begin to diverge. Nevertheless, a clear scale dependence emerges from this analysis.

We see that within each band the observed negative turbulent air–sea feedback on SO SST anomalies weakens from the grid scale ($\leq 0.1$ SU) across the synoptic scales (5°–30° longitude, ~5–30 SU) to the basin scales (60°–120° longitude, ~60–120 SU). The magnitude of this weakening is typically $5\,W\,m^{-2}\,K^{-1}$, and is observed to be the same in all three bands considered in Fig. 5a. As scales increase out to the circumpolar scale (360° longitude, ~360 SU), the results are more ambiguous and indicate, for the two higher-latitude ACC

bands, a restrengthening of the feedback. At these largest scales, the two realizations shown in Fig. 5 for each scale, often spread significantly, suggesting that results are less robust in that regime. Appendix A provides further discussion of this aspect. In the following we focus on variability on basin scales and smaller ($\leq 90°$ longitude), for which the scale dependence of the air–sea feedback is systematic across the SO.

In the poleward-most ACC band at approximately 55°S, the two sets of ERA-I results based on including $Q$ for sea ice concentrations $c \leq 15\%$ (filled circles) or only for $c = 0\%$ (filled diamonds) are discernible. Importantly, however, both estimates are qualitatively similar,

and both yield a robust scale dependence of the air–sea feedback. The slightly larger values of the $c = 0\%$ based estimate likely reflect its lower average latitude.

Poleward of this ACC band at about 55°S, seasonal sea ice prevails throughout the wintertime and in most of spring and fall. In late summer (JFM), however, the region between the −1°C October and 0°C February SST is consistently sea ice free (cf. bright red and black dashed contours in, e.g., Fig. 1), allowing for an estimate of the air–sea feedback acting on summertime $T'$ in this region of seasonal sea ice. Note that in the maps of Fig. 4a the seasonal DJF feedback remains mostly unavailable in this region, as a large number of months per year (i.e., NDJF SST and DJFM heat flux data) are used. Here the summertime (February) $\alpha$ is estimated as in (2), taking time $t$ only in months January and February (i.e., from JF SST and FM heat flux data). This is displayed by the blue dots in Fig. 5c, along with the summertime air–sea feedback estimated for the three isotherm bands of Fig. 5a. We see that summertime feedbacks (Fig. 5c) in the latter bands are typically slightly weaker than the feedbacks estimated from year-round time series (that is including all months of the year, Fig. 5a), falling to only approximately 5 W m$^{-2}$ K$^{-1}$ in the poleward-most band at large scales. The systematic poleward weakening of the turbulent air–sea feedback (from red to blue marker shades), which is observed year-round (Fig. 5a), continues on across the wintertime sea ice edge into the region of seasonal sea ice in the summertime (Fig. 5c). In this region, and in the summertime, the data reveal a decrease of the air–sea feedback from grid to basin scales that is comparable to that obtained further equatorward, and from year-round data.

This scale dependence holds even when considering simple zonal bands instead of streamline bands. This is shown for the two bands 30°–50°S and 50°–70°S in Fig. 5b for year-round, and in Fig. 5d for summertime observations. The general features of the scale dependence described here are also robust when considering OAFlux instead of ERA-I data, as shown by the open markers in each of the panels of Fig. 5.

The next section assesses the implications of these new estimates of a scale-dependent SO air–sea feedback for the decay of SH SST anomaly patterns, providing a discussion of the physical mechanisms at play. As emphasized in the introduction section, we will be particularly interested in SST perturbations induced adjacent to the Antarctic seasonal sea ice in the summertime on large spatial scales. As seen from Fig. 5c, these are subject to feedbacks as low as approximately 5 W m$^{-2}$ K$^{-1}$ suggesting they are rather weakly damped by air–sea interactions.

## 6. Physical mechanisms and implications for decay time scales of SO SST patterns

The implications of the air–sea feedbacks presented above for air–sea decay time scales of SO SST signals are assessed in Fig. 6. Variations of the observed turbulent feedback $\alpha$ as a function of background SST for latitude, month, and spatial scale are summarized by the colored markers in Fig. 6a. These are used, together with streamline averages of the climatological mixed layer depth $\overline{h}$ (indicated by black crosses in Fig. 6b), to construct a monthly, scale-dependant climatology of the air–sea damping time scale $\tau = \rho c_p \overline{h} / \alpha$ displayed by the colored markers in Fig. 6b. The three separate panels of Figs. 6a,b display results for the three isotherm bands of Fig. 5a (contoured bright red in Fig. 1), moving equatorward, from left to right, from the coldest band adjacent to Antarctic sea ice across the ACC toward warmer isotherms. Note that the month of year varies along the horizontal axes, and spatial scale increases from cold to warm colors. We see that air–sea turbulent fluxes act to damp SSTs throughout the SO at all spatial scales and in all months at rates varying between 25 and 5 W m$^{-2}$ K$^{-1}$ (colored markers in Fig. 6a), leading to air–sea damping times $\tau$ ranging from a season up to approximately 1.5 yr (colored markers in Fig. 6b).

In the following we place these estimates in the context of the other physical mechanisms inducing decay of SST anomalies. Locally SST anomalies are "damped" via mean-flow advection, and the magnitude of this advective damping rate can be scaled as $\tau_{adv}^{-1} = U/L$. This is displayed by the asterisks in Fig. 7 as function of SST anomaly spatial scale $L$ and for typical SO background flow speeds $U$ between 1 and 10 cm s$^{-1}$. We see that, at the 100-km scale, local advective damping is fast (~1 month), at synoptic scales (500–1000 km) it is comparable to air–sea damping (~3–24 months), and at basin scales (>6000 km) it becomes negligible in comparison (>2 yr).

Next let us consider the decay of a SST anomaly pattern $T'$, induced along an ACC streamline band at a given spatial scale and in a given season, following the circumpolar flow (denoted by $d_t$). This can be written as

$$\rho c_p \overline{h} d_t T' = -\alpha_{total} T' = -(\alpha_{mix} + \alpha + \alpha_{sub}) T'. \quad (3)$$

We see that, following the flow, decay results from (negative) feedbacks on SST induced by lateral surface mixing due to turbulent eddies $\alpha_{mix}$, air–sea interaction $\alpha$, and interactions with the subsurface ocean (e.g., entrainment) $\alpha_{sub}$. Here it is important to note that the feedback due to air–sea interaction $\alpha$ (displayed in e.g., Fig. 6a), although it is obtained by applying (2) locally, is not affected by the large advective damping rates
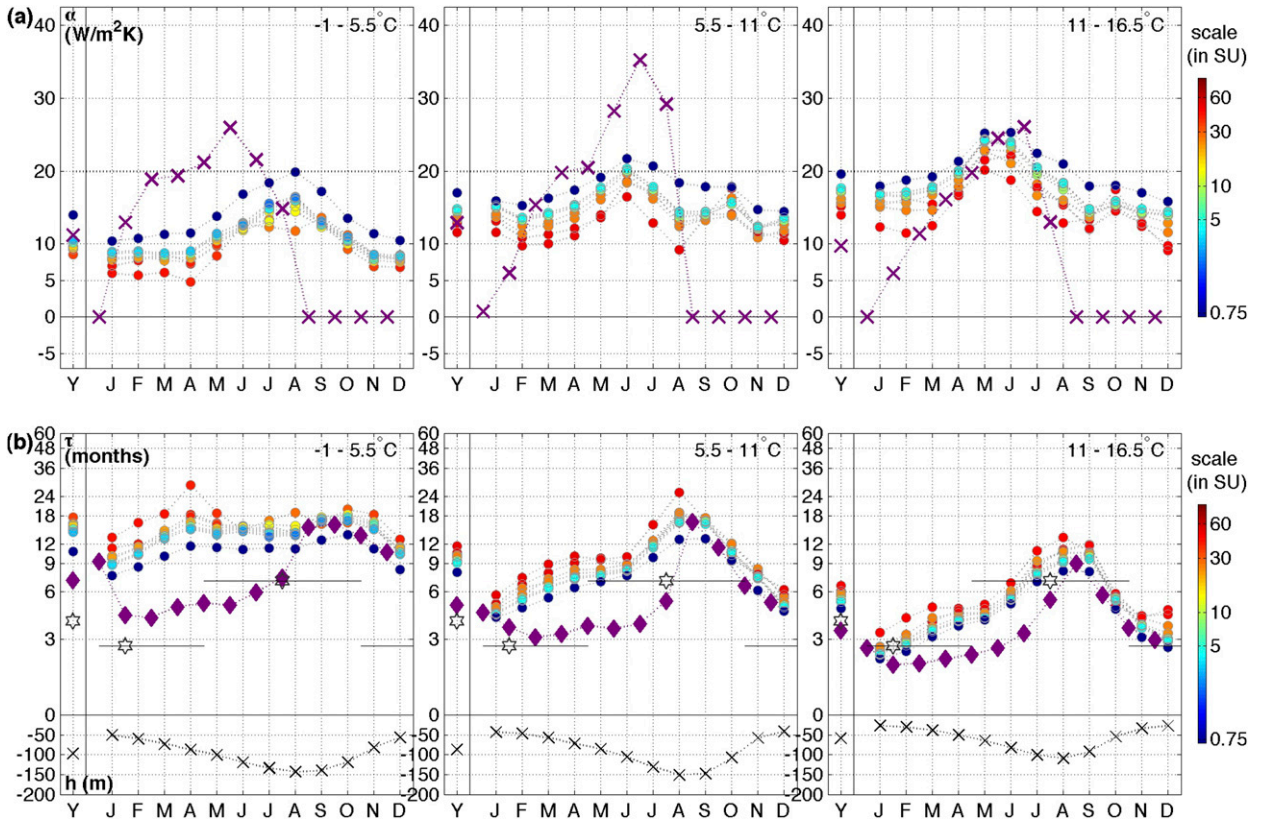
FIG. 6. (a) SO turbulent air–sea feedback $\alpha$ (vertical axes, W m$^{-2}$ K$^{-1}$; based on ERA-I, with $c > 0\%$ masking of $Q$) as a function of season [horizontal axes: year-round (Y) and monthly (J, F, M, etc.) values] and spatial scale (colors indicate the scale-specific area in SU, increasing from the grid scale, at <0.75 SU, to the basin scale, at 90 SU). The three panels display results for three SO isotherm bands (also used in Figs. 5a,c, and defined in terms of October SST as indicated by the text in the panels). Purple crosses show, for comparison, an estimate of the entrainment feedback $\alpha_{\text{entr}}$, as induced by the seasonal progression of the SO mixed layer depth $\overline{h}$ [black crosses in (b), m]. (b) The associated time scale $\tau = \rho_o c_p \overline{h}/\alpha$ (months) resulting from air–sea feedback alone (colored markers), or from combined air–sea and entrainment feedbacks (purple diamonds—here, for clarity, only one spatial scale, the 10-SU scale, approximately 10° × 10°, is displayed). Observed $e$-folding time scales of SAM-associated SH SST patterns, as reported by Ciasto and Thompson (2008) from year-round, warm and cold season data, are indicated by stars.

discussed above (asterisks in Fig. 7).[1] Note that in the presence of sea ice $\alpha_{\text{total}}$ in (3) furthermore contains a contribution from ocean to sea ice heat fluxes providing a negative feedback on SST, which acts in addition to that by ocean–atmosphere fluxes (i.e., $\alpha$), and whose magnitude remains to be quantified observationally. A scaling-type estimate of $\alpha_{\text{mix}} = \rho c_p h \tau_{\text{mix}}^{-1}$ is provided by the colored markers in Fig. 7. In this the damping rate due to surface mesoscale eddy-driven

mixing is obtained as $\tau_{\text{mix}}^{-1} = \kappa/L^2$, using a typical range of the SO surface eddy diffusivity for SST $\kappa$ (cf. Marshall et al. 2006; Shuckburgh et al. 2011; Abernathey and Marshall 2013). We see that, whereas, at the 100-km scale, the impact of mixing on the decay of a SST anomaly pattern along the ACC flow is comparable to that of air–sea damping (~2–9 months), as spatial scales increase beyond 500 km the impact of mixing is negligible in comparison (>5 yr).

Air–sea feedbacks may thus be the primary player in the decay of SST anomalies along the ACC flow. Figure 6b shows that SST anomaly patterns induced at basin scales (~90° longitude, red circles) can persist typically 3 months to more than half a year longer than those induced at the grid scale (blue circles), before being damped to the atmosphere. This stems from the observed weakening of the turbulent heat flux feedback (Fig. 6a) by 5 W m$^{-2}$ K$^{-1}$ from grid (blue) to basin (red) scales. The magnitude of this scale dependence, which is

---

[1] This is discussed by FK02, and can be understood as follows. Diagnosis of $\alpha$ is based upon the relationship $Q' = F' + \alpha T'$, and the analysis, at lags larger than the persistence time of the atmospheric stochastic air–sea heat flux forcing $F'$ (of typically a few days; e.g., Frankignoul 1985; Frankignoul et al. 1998), of its lagged covariance with $T'$, weighted, as specified via (2), by the decay of the $T'$ autocovariance itself (cf. section 2 and appendix A). This yields the air–sea feedback rate $\alpha$, independent of the mechanisms inducing the local $T'$ decay.
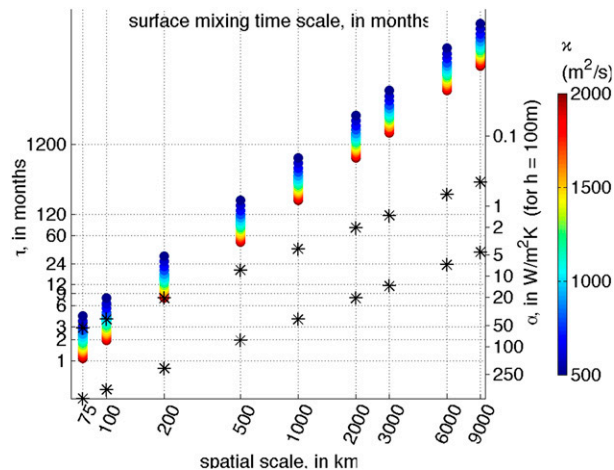
FIG. 7. SST surface mixing time scale as function of spatial scale of the SST anomaly (horizontal axis, km) for typical SO surface mixing rates $\kappa$ from 500 to 2000 $m^2 s^{-1}$ (colors), typical of the range observed upon moving from the ACC core to its equatorward edge and subtropical western boundary and Agulhas Return Current systems, as derived by Marshall et al. (2006). Asterisks indicate the local SST damping time scales and equivalent feedback rates induced by advection by a mean flow of 1 and 10 cm $s^{-1}$. The right-hand vertical axis indicates the equivalent feedback strengths (W $m^{-2} K^{-1}$) obtained for a 100-m-deep surface mixed layer.

similar to that reported for the NH basins by FK02, is not particularly strong. Variations of the turbulent air–sea feedback with season and especially latitude are seen to be of comparable magnitude in Fig. 6a. The observed summertime reduction in the air–sea feedback $\alpha$ is outweighed by the shallowing mixed layers resulting in a summertime minimum in observed air–sea decay time scales $\tau$ in Fig. 6b. In the SH subtropics (Fig. 6b, right), SST anomaly patterns, induced in the summertime, decay in amplitude within three months due to air–sea interaction, that is by fall–beginning of winter. In contrast, along the equatorward ACC branches (Fig. 6b, center) weakened air–sea damping allows them to typically "survive" around half a year following the flow, through to the middle–end of winter. In the poleward-most SO band adjacent to the zone of seasonal sea ice (Fig. 6b, left), summer-induced SST patterns can survive even longer, typically around and in excess of one year.[2]

---

[2] Note here that $\tau^{-1}$ quantifies the air–sea SST damping rate acting in a given season and that the evolution due to air–sea damping of a SST anomaly induced in a given season results from the convolution of $\tau$ throughout the following seasons. Given the summer-to-winter decrease of damping rates, a summertime-forced SST anomaly thus persists at least as long as indicated by summertime $\tau$ under the action of air–sea interaction alone (reversely, a winter-forced anomaly persists at most as long as wintertime $\tau$).

This stark latitudinal contrast is set by a cooperation of weakening air–sea feedbacks (Fig. 6a) observed moving poleward across the SO and the overall deeper mixed layers (crosses in Fig. 6b) in the ACC bands (center and right panels). This is seen in the maps of air–sea damping times applying to the grid scale (Fig. 4b), and Fig. 6b establishes that it also applies on basin scales.

The stars in Fig. 6b indicate, for comparison, the observed persistence time of the SH SST anomaly pattern forced by the SAM, as derived from year-round, warm and cold season observations by Ciasto and Thompson (2008). These authors rationalize the observed decay times in terms of air–sea damping alone, with its seasonality set by that of observed SH mixed layer depths, in the presence of a constant air–sea feedback of 20 W $m^{-2} K^{-1}$. Here we have shown from observations that $\alpha < 20$ W $m^{-2} K^{-1}$ in the SO on the spatial scales of SAM-type SST: $\alpha$ barely reaches 20 W $m^{-2} K^{-1}$ at its observed wintertime peak in the warmest SO isotherm band (Fig. 6a, right). Along the ACC and especially adjacent to the sea ice (center and left panels), air–sea feedbacks reach only 5–15 W $m^{-2} K^{-1}$. Air–sea decay time scales (colored markers in Fig. 6b) around Antarctica are thus several times longer than the decay times of observed SH-wide SAM-induced SST patterns (stars in Fig. 6b).

Since mean-flow advection and surface mixing are both not anticipated to play an important role in shortening large-scale SO SST persistence, there are two main interpretations for this mismatch. First, the observed hemisphere-wide (20°–80°S) SAM–SST regression reported in Ciasto and Thompson (2008) might primarily reflect lower SH latitudes. This aspect can be examined easily using a streamline-wise analysis of the SAM–SST persistence, building upon the study by Ciasto et al. (2011), and it would be interesting to assess this explicitly as a function of spatial scale in further study. Second, air–sea interaction alone may not be a sufficient damping mechanism, in which case subsurface feedback processes, $\alpha_{sub}$ in (3), must be at work.

The feedback $\alpha_{sub}$ may act to enhance the persistence of SST anomalies from winter to winter, thus providing a seasonally acting positive feedback on SST, via re-emergence, as detected observationally in parts of the SH—for example, in the southwestern Pacific by Ciasto and Thompson (2009). However, it is also anticipated to provide a negative feedback, via entrainment of unmodified waters from the seasonal thermocline below. A simple scaling-type estimate of this contribution to the subsurface feedback, which we will refer to as $\alpha_{entr}$, is given by the purple crosses in Fig. 5a. Neglecting contributions by lateral induction, vertical advection, and anomalies in mixed layer depth, it is obtained simply

from the seasonal progression of $\overline{h}$ within the various SO bands as $\alpha_{\text{entr}} = \rho c_p \partial_t \overline{h}$ [see also Frankignoul (1985)]. We see that the presence of a seasonal cycle in mixed layer depth induces a negative feedback on SST, originating from the seasonal thermocline. It is comparable in magnitude to the air–sea feedback $\alpha$ in its annual mean, and stems only from its action during the summer-to-winter entraining season of deepening mixed layers. During this time $\alpha_{\text{entr}}$ can exceed $\alpha$ by up to a factor of 2. An estimate of the SST decay time scale resulting from the combined action of entrainment and air–sea interaction $\tau = \rho c_p \overline{h} / (\alpha + \alpha_{\text{entr}})$ is provided by the filled purple diamonds in Fig. 5b (displayed for the ~1000-km scale only for clarity). We see that from late summer through the middle of winter the addition of entrainment acts to reduce SST decay time scales by more than half with respect to air–sea interaction alone (colored markers), providing a closer match to the observed SAM SST decay time scales (stars). This finding is overall consistent with the results of Verdy et al. (2006), who require a feedback of $20 \, \text{W} \, \text{m}^{-2} \, \text{K}^{-1}$ in addition to the air–sea feedback in order to realistically simulate SST variability following the ACC flow. This is of special interest, since, if the observed rather rapid decay of summertime SAM-induced SST perturbations (stars in Fig. 6b) is indeed representative of the high-latitude SO, this may mitigate the impact of summertime SAM forcing in preconditioning sea ice growth at the beginning of the following winter.

## 7. Conclusions

In this paper we have presented first estimates of SO air–sea heat flux feedback strengths and associated SST damping time scales and their dependence on season and spatial scale. Two datasets of heat flux and SST are used, yielding broadly similar results. Air–sea interaction damps SST anomalies in all regions of the SO and all seasons, at rates varying from approximately $20 \, \text{W} \, \text{m}^{-2} \, \text{K}^{-1}$ in the subtropics falling to approximately $5\text{–}15 \, \text{W} \, \text{m}^{-2} \, \text{K}^{-1}$ over the ACC and around Antarctica (see Figs. 1 and 6a). The air–sea feedback is found to be overall smaller in the summer than in the winter, by approximately $5 \, \text{W} \, \text{m}^{-2} \, \text{K}^{-1}$ in the circumpolar average (Figs. 4a and 6a). It also features a discernible, but modest, longitudinal scale dependence characterized by an approximate $5 \, \text{W} \, \text{m}^{-2} \, \text{K}^{-1}$ reduction in strength moving out from the resolution of the data ($\geq 1°$) to basin scales (Fig. 5). The feedback is controlled by turbulent latent heat fluxes, with sensible and radiative processes typically playing a much lesser role (Figs. 1 and 3).

Our study is of particular interest and relevance to understanding the persistence of SST anomalies generated by the SAM, the leading mode of atmospheric variability

around Antarctica. We find that the observed air–sea feedback on summertime SAM-like SST signals around Antarctica is typically $5\text{–}12 \, \text{W} \, \text{m}^{-2} \, \text{K}^{-1}$. If this acts over a mixed layer depth of typically 50 m, air–sea damping time scales of typically 6–16 months are implied (see Figs. 4c and 6b). Observed SST decay time scales are only about 4 months suggesting that processes other than air–sea interaction must be at play. Whereas mean-flow advection and eddy-driven mixing are anticipated to have a negligible impact at these basin-wide scales (with associated damping time scales of $\geq 2$ and 100 yr, respectively, for typical ACC mean flows and surface diffusivities, and at spatial scales $\geq 60°$ longitude), entrainment of subsurface properties from the seasonal thermocline, which "dilutes" the signal imprinted by the summertime SAM, is found to provide a large negative feedback on summertime-induced SST. It is quantified to average to approximately $20 \, \text{W} \, \text{m}^{-2} \, \text{K}^{-1}$ over the summer-to-winter entraining season and to reduce SST persistence time scales by more than half with respect to the prediction based on large-scale air–sea interaction alone.

This discussion should also be seen in the context of the modeling study of Ferreira et al. (2015), who report damping time scales of SAM-induced anomalies of nearly 3 yr (in MITgcm) and, more realistically, 7 months (in CCSM3.5). We conclude that observed values of air–sea damping reported here lie closer to those acting in CCSM3.5 than in the simplified MITgcm configuration, which employs a highly idealized geometry. In this context it is important to note, however, that the direct observational data content underlying our observation-based assessment of the SST air–sea feedback in the SO remains scarce in terms of air–sea fluxes, highlighting the urgent need for improved observational flux datasets at high latitudes (see e.g., Dong et al. 2010; Bourassa et al. 2013).

Finally, our study suggests a number of profitable avenues for further research as datasets improve. In our focus on the seasonality and scale dependence of the air–sea feedback, we have directed our attention to turbulent fluxes, which typically dominate. However, around Antarctica, where the net feedback itself is small, radiative fluxes make an increasingly important contribution with implications that we have not examined, or discussed here. This may be of particular importance in relation to cloud feedback processes associated with SAM forcing as examined by Grise et al. (2013). As coupled modeling studies are increasingly used to obtain insight on climate, and in particular SO processes, an assessment of the modeled air–sea feedbacks over the SO with respect to the observations presented here would be useful. One such comparative study is presented by Frankignoul et al. (2004) for the ocean basins north of Drake Passage.
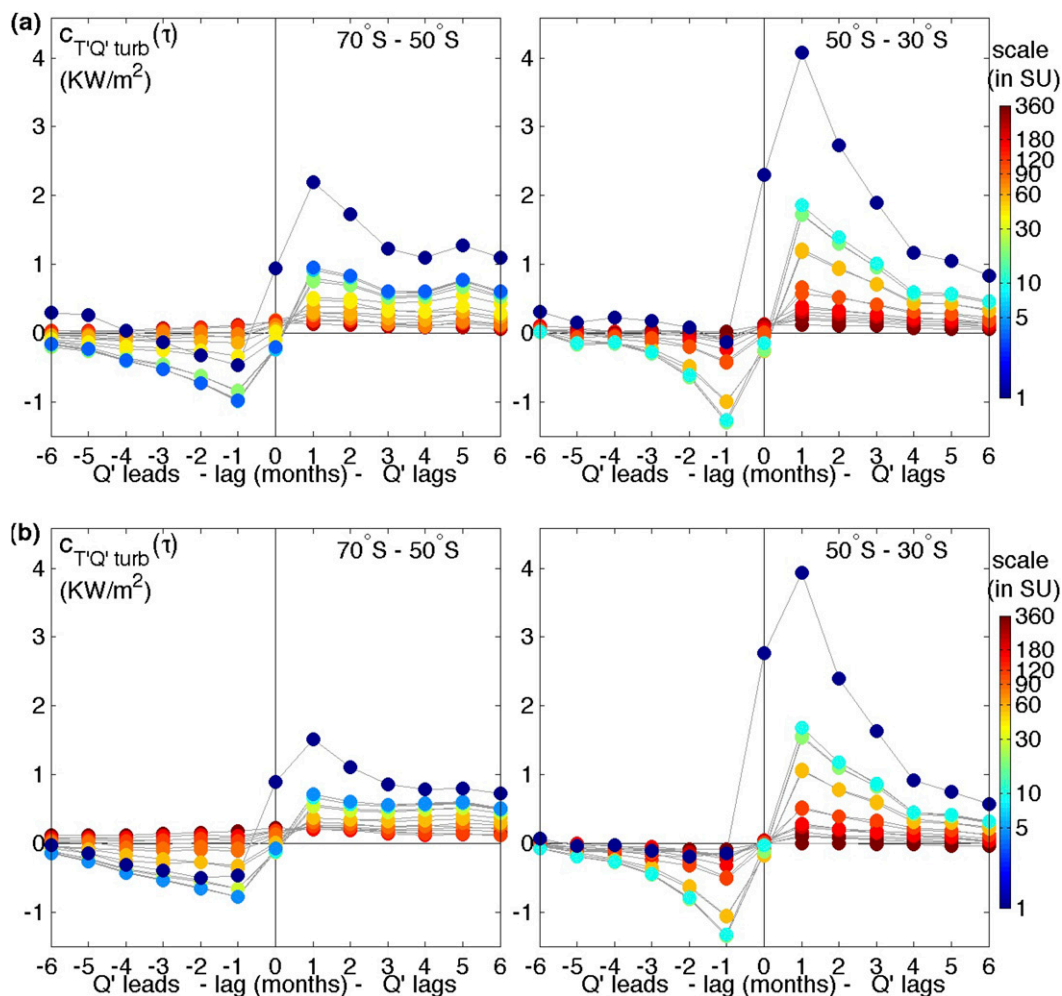
FIG. A1. The lagged covariance between $T'$ and turbulent $Q'$ (positive upward), revealing, at negative and positive lags, respectively, the signature of $Q'$ forcing and feeding back on $T'$, as observed at various spatial scales. The colors indicate the area of the scale-specific coarse-grid boxes (in the area unit SU, as in Fig. 6). It increases from the grid scale, at $\sim$0.1 SU, to the circumpolar scale, at $\sim$360 SU. Displayed are the two latitude bands of Figs. 5b,d. Results are based on (a) ERA-I data (using $c > 0\%$ masking of $Q$) and (b) OAFlux data.

The contrasting air–sea feedback strengths reported here between midlatitude western boundary current regimes and the circumpolar channel of the ACC will be discussed in more detail in a companion paper. There we will also study the mechanisms underlying the observed scale dependence of the air–sea feedback. Further study will moreover benefit from the growing observational record of satellite SST and Argo data and allow to quantify more robustly the feedback processes on SST originating from the seasonal thermocline.

## APPENDIX A

### The Scale Dependence of Forcing and Feedback Contributions to SO Air–Sea Heat Fluxes

To further investigate SO air–sea heat flux feedbacks and their dependence on spatial scale, we examine the covariance function $c_{TQ}(i) = \overline{T'(t)Q'(t + i\delta t)}$ as function of lag ($i$, in months). It is displayed in Fig. A1 for various SO bands (as indicated by the text in the panels). Figures A1a and A1b show that ERA-I and OAFlux-based

$T'$ and $Q'$ time series feature very similar covariance functions across the range of spatial scales considered (indicated by the color bar). At positive lags ($i > 0$) of 1–3 months, $c_{TQ}$ reveals the signature of the $Q'$ response to $T'$ and is observed to decrease systematically from the grid scale (blue) all the way up to the circumpolar scale (red). Variances of $T'$ and $Q'$ (not shown) also decrease systematically across all spatial scales. At the largest spatial scales, the estimate (2) of $\alpha$, displayed in Fig. 5, thus results from the division of two very small numbers.

Figure A1, moreover, shows that, at spatial scales smaller than approximately 90° longitude, $c_{TQ}$ is observed to change sign between positive and negative lags, displaying a negative peak at small negative lags, which is the signature of $Q'$ forcing $T'$. This signature is, as expected, observed to be most pronounced at the synoptic scales (5°–30° longitude). At the grid scale, the signature of heat flux forcing of SST variability is weaker, and near absent in the lower SH latitudes (right panels), suggesting that here ocean dynamics (such as Agulhas meanders, etc.) are a primary forcing agent of grid-scale SST variability. At larger than synoptic scales, the heat flux forcing signature is also observed to weaken. It remains clearly visible out to basin scales (60°–90° longitude). At the largest near-circumpolar scales, however, $c_{TQ}$ is observed to be weakly positive for both positive and negative lags, indicating that turbulent $Q'$ do not systematically contribute to forcing $T'$ at circumpolar scales. Here $T'$ dynamics thus differ from those dominating variability at synoptic to basin scales, for which the $\alpha$ diagnostic (2), used here, has been developed. Consistent with the absence of a change of sign in $c_{TQ}$, the residual low-frequency content of $Q'$ (as measured by its lag-1 autocorrelation, not shown) is large at these large scales, further questioning the validity of the diagnostic in this regime. However, because the forcing contribution does not dominate $Q'$ variability at these scales, the sense of the bias in the estimate is unclear. Further study is thus necessary to establish whether the observed increase of the air–sea feedback from basin to circumpolar scales suggested in Fig. 5 is a real feature or an artifact of the analysis technique.

## APPENDIX B

### Error on the Estimation of the Air–Sea Feedback $\alpha$

The calculation in (2) relies on perfect knowledge of the covariance function between anomalies in air–sea fluxes and SST, as well as perfect knowledge of the latter's autocovariance function. These functions are only approximately known because of the finite size of the time series used and this introduces an error in the estimation of $\alpha$. To obtain an estimate of the latter, we have repeated $N$ times the calculation of $\alpha$ in a simple stochastic model, each simulation being 34 yr long. The model for the SST anomaly $T'$, forced by stochastic variability in the (upward) surface heat flux $Q'$ is written as

$$\rho c_p h \frac{dT'}{dt} = F' - (\alpha + \alpha_{\text{entr}})T', \quad \text{(B1)}$$

where $\alpha_{\text{entr}}$ is the feedback due to entrainment; $\rho$, $c_p$, and $h$ have been introduced earlier; and the surface heat flux anomaly $Q' = -(F' - \alpha T')$ (positive upward) has been decomposed into a stochastic component $F'$ and a component responding to the SST anomaly (the heat flux feedback effect $\alpha T'$). Modeling $F'$ as a first-order Markov process with a short decorrelation time [of a few days, see Frankignoul (1985)], $N$ realizations of the model are produced, that is, $N$ monthly time series of $T'$ and $Q'$, each 34 yr long. For each time series of the model output $\alpha$ is reconstructed by application of (2), thereby producing a distribution of $N$ values for the empirically estimated $\alpha$. As an example, for $N = 1000$ and a typical set of parameters $\alpha = \alpha_{\text{entr}} = 10\,\text{W m}^{-2}\,\text{K}^{-1}$ and $h = 100\,\text{m}$, one finds that the most likely value for the reconstructed $\alpha$ oscillates around the true value ($10\,\text{W m}^{-2}\,\text{K}^{-1}$), while the standard deviation of the distribution typically is approximately 5–$6\,\text{W m}^{-2}\,\text{K}^{-1}$. This suggests that the error due to the sampling size is on the order of 50% (a similar result is found for different values of the parameters).

## REFERENCES

Abernathey, R. P., and J. Marshall, 2013: Global surface eddy diffusivities derived from satellite altimetry. *J. Geophys. Res. Oceans*, **118**, 901–916, doi:10.1002/jgrc.20066.

Bladé, I., 1997: The influence of midlatitude ocean–atmosphere coupling on the low-frequency variability of a GCM. Part I: No tropical SST forcing. *J. Climate*, **10**, 2087–2106, doi:10.1175/1520-0442(1997)010<2087:TIOMOA>2.0.CO;2.

Bourassa, M. A., and Coauthors, 2013: High-latitude ocean and sea ice surface fluxes: Challenges for climate research. *Bull. Amer. Meteor. Soc.*, **94**, 403–423, doi:10.1175/BAMS-D-11-00244.1.

Bretherton, F. P., 1982: Ocean climate modeling. *Prog. Oceanogr.*, **11**, 93–129, doi:10.1016/0079-6611(82)90005-2.

Ciasto, L. M., and D. W. J. Thompson, 2008: Observations of large-scale ocean–atmosphere interaction in the Southern Hemisphere. *J. Climate*, **21**, 1244–1259, doi:10.1175/2007JCLI1809.1.

——, and ——, 2009: Observational evidence of reemergence in the extratropical Southern Hemisphere. *J. Climate*, **22**, 1446–1453, doi:10.1175/2008JCLI2545.1.

——, M. A. Alexander, C. Deser, and M. H. England, 2011: On the persistence of cold-season SST anomalies associated with the annual modes. *J. Climate*, **24**, 2500–2515, doi:10.1175/2010JCLI3535.1.

de Boyer Montégut, C., 2008: Mixed layer depth climatology and other related ocean variables. IFREMER, accessed 6 January 2014. [Available online at www.ifremer.fr/cerweb/deboyer/mld/Surface_Mixed_Layer_Depth.php.]

——, G. Madec, A. S. Fischer, A. Lazar, and D. Iudicone, 2004: Mixed layer depth over the global ocean: An examination of profile data and a profile-based climatology. *J. Geophys. Res.*, **109**, C12003, doi:10.1029/2004JC002378.

Dee, D. P., and Coauthors, 2011: The ERA-Interim reanalysis: Configuration and performance of the data assimilation system. *Quart. J. Roy. Meteor. Soc.*, **137**, 553–597, doi:10.1002/qj.828.

Dong, S., J. Sprintall, S. T. Gille, and L. Talley, 2008: Southern Ocean mixed-layer depth from Argo float profiles. *J. Geophys. Res.*, **113**, C06013, doi:10.1029/2006JC004051.

——, S. T. Gille, J. Sprintall, and E. J. Fetzer, 2010: Assessing the potential of the Atmospheric Infrared Sounder (AIRS) surface temperature and specific humidity in turbulent heat flux estimates in the Southern Ocean. *J. Geophys. Res.*, **115**, C05013, doi:10.1029/2009JC005542.

Ferreira, D., C. Frankignoul, and J. Marshall, 2001: Coupled ocean–atmosphere dynamics in a simple midlatitude climate model. *J. Climate*, **14**, 3704–3723, doi:10.1175/1520-0442(2001)014<3704:COADIA>2.0.CO;2.

——, J. Marshall, C. M. Bitz, S. Solomon, and A. Plumb, 2015: Antarctic Ocean and sea ice response to ozone depletion: A two-time-scale problem. *J. Climate*, **28**, 1206–1226, doi:10.1175/JCLI-D-14-00313.1.

Frankignoul, C., 1985: Sea surface temperature anomalies, planetary waves, and air–sea feedback in the middle latitudes. *Rev. Geophys.*, **23**, 357–390, doi:10.1029/RG023i004p00357.

——, and K. Hasselmann, 1977: Stochastic climate models. Part II: Application to sea-surface temperature anomalies and thermocline variability. *Tellus*, **29A**, 289–305, doi:10.1111/j.2153-3490.1977.tb00740.x.

——, and E. Kestenare, 2002: The surface heat flux feedback. Part I: Estimates from observations in the Atlantic and the North Pacific. *Climate Dyn.*, **19**, 633–647, doi:10.1007/s00382-002-0252-x.

——, A. Czaja, and B. L'Heveder, 1998: Air–sea feedback in the North Atlantic and surface boundary conditions for ocean models. *J. Climate*, **11**, 2310–2324, doi:10.1175/1520-0442(1998)011<2310:ASFITN>2.0.CO;2.

——, E. Kestenare, M. Botzet, A. F. Carril, H. Drange, A. Pardaens, L. Terray, and R. Sutton, 2004: An intercomparison between the surface heat flux feedback in five coupled models, COADS and the NCEP reanalysis. *Climate Dyn.*, **22**, 373–388, doi:10.1007/s00382-003-0388-3.

Grise, K. M., L. M. Polvani, G. Tselioudis, Y. Wu, and M. D. Zelinka, 2013: The ozone hole indirect effect: Cloud radiative anomalies accompanying the poleward shift of the eddy driven jet in the southern hemisphere. *Geophys. Res. Lett.*, **40**, 3688–3692, doi:10.1002/grl.50675.

Hausmann, U., and A. Czaja, 2012: The observed signature of mesoscale eddies in sea surface temperature and the associated heat transport. *Deep-Sea Res. I*, **70**, 60–72, doi:10.1016/j.dsr.2012.08.005.

Holte, J., and L. Talley, 2009: A new algorithm for finding mixed layer depths with applications to Argo data and Subantarctic Mode Water formation. *J. Atmos. Oceanic Technol.*, **26**, 1920–1939, doi:10.1175/2009JTECHO543.1.

Marshall, J., E. Shuckburgh, H. Jones, and C. Hill, 2006: Estimates and implications of surface eddy diffusivity in the Southern Ocean derived from tracer transport. *J. Phys. Oceanogr.*, **36**, 1806–1821, doi:10.1175/JPO2949.1.

Park, S., C. Deser, and M. A. Alexander, 2005: Estimation of the surface heat flux response to sea surface temperature anomalies over the global oceans. *J. Climate*, **18**, 4582–4599, doi:10.1175/JCLI3521.1.

Rahmstorf, S., and J. Willebrand, 1995: The role of temperature feedback in stabilizing the thermohaline circulation. *J. Phys. Oceanogr.*, **25**, 787–805, doi:10.1175/1520-0485(1995)025<0787:TROTFI>2.0.CO;2.

Schmidtko, S., G. C. Johnson, and J. M. Lyman, 2013: MIMOC: A global monthly isopycnal upper-ocean climatology with mixed layers. *J. Geophys. Res. Oceans*, **118**, 1658–1672, doi:10.1002/jgrc.20122.

Shuckburgh, E., G. Maze, D. Ferreira, J. Marshall, H. Jones, and C. Hill, 2011: Mixed layer lateral eddy fluxes mediated by air–sea interaction. *J. Phys. Oceanogr.*, **41**, 130–144, doi:10.1175/2010JPO4429.1.

Thompson, D. W. J., S. Solomon, P. J. Kushner, M. H. England, K. M. Grise, and D. J. Karoly, 2011: Signatures of the Antarctic ozone hole in Southern Hemisphere surface climate change. *Nat. Geosci.*, **4**, 741–749, doi:10.1038/ngeo1296.

Verdy, A., J. Marshall, and A. Czaja, 2006: Sea surface temperature variability along the path of the Antarctic Circumpolar Current. *J. Phys. Oceanogr.*, **36**, 1317–1331, doi:10.1175/JPO2913.1.

Yu, L., X. Jin, and R. A. Weller, 2008: Multidecade global flux datasets from the Objectively Analyzed Air-sea Fluxes (OAFlux) project: Latent and sensible heat fluxes, ocean evaporation, and related surface meteorological variables. Woods Hole Oceanographic Institution, OAFlux Project Tech. Rep. OA-2008-01, 64 pp.